Contents lists available at ScienceDirect

Nuclear Instruments and Methods in Physics Research A

Hexagonal boron nitride thin film thermal neutron detectors with high energy resolution of the reaction products

T.C. Doan, S. Majety, S. Grenadier, J. Li, J.Y. Lin, H.X. Jiang*

Department of Electrical & Computer Engineering, Texas Tech University, Lubbock, TX 79409, United States

ABSTRACT

Hexagonal boron nitride (h-BN) is highly promising for solid-state thermal neutron detector applications due to its many outstanding physical properties, especially its very large thermal neutron capture cross-section ($\sim$3840 barns for ^{10}B), which is several orders of magnitude larger than those of most other isotopes. The focus of the present work is to carry out studies on h-BN thin film and detector properties to lay the foundation for the development of a direct-conversion solid-state thermal neutron detector with high sensitivity. The measured carrier mobility-lifetime ($\mu\tau$) product of h-BN thin films grown on sapphire substrates is 2.83×10^{-7} cm^2/V for electrons and holes, which is comparable to the value of about 10^{-7} cm^2/V for GaN thin films grown on sapphire. Detectors based on h-BN thin films were fabricated and the nuclear reaction product pulse height spectra were measured. Under a bias of 20 V, very narrow individual peaks corresponding to the reaction product energies of α and Li particles as well as the sum peaks have been clearly resolved in the pulse height spectrum for the first time by a B-based direct-conversion semiconductor neutron detector. Our results indicate that h-BN thin film detectors possess unique advantages including small size, low weight, portability, low voltage operation and high energy resolution of specific reaction products.
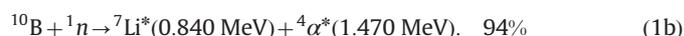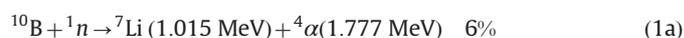
© 2015 Elsevier B.V. All rights reserved.

1. Introduction

Hexagonal boron nitride (h-BN) is a wide bandgap semiconductor ($E_g \sim 6.5$ eV). It has attracted considerable attention due to its potential for deep ultraviolet photonic device applications [1–5] and for its utility in exploring new physical properties in two dimensional (2D) systems that are complementary to graphene [6–8]. h-BN is also very promising for solid-state thermal neutron detector applications [9,10] due to its very large thermal neutron capture cross-section ($\sim$3840 barns for ^{10}B), which is several orders of magnitude larger than those of most other isotopes [11,12]. Although ^{3}He gas detectors have long been the preferred choice for neutron detection, they have many disadvantages such as high cost, large volume, low Q value ($\sim$ 0.764 MeV), high voltage operation, and very high ionization energy. Moreover, there continues to be a need to "develop alternative detection technologies that do not require ^{3}He gas to enable the United States to devote the scarce supplies of ^{3}He [13] to those applications where no substitutes are possible" [14]. Solid-state thermal neutron detectors have recently been rapidly developed for their obvious advantages including independence from ^{3}He gas, compactness, and low voltage operation [15–26]. For h-BN neutron detectors, the neutron capture, charge

generation and collection, electrical signal generation occur in the same h-BN epilayer. Therefore, h-BN detectors are direct conversion neutron detectors and are potentially capable of providing very high detection efficiencies (approaching 100%) for thermal neutrons. Another distinct advantage of h-BN detectors is that they have a negligible response to γ-photons [10]. This is to be expected as BN is composed of low atomic number elements, B(5) and N(7), BN's interaction with γ rays should be low.

In h-BN, after a ^{10}B atom captures a thermal neutron, the following nuclear reactions occur:

$$^{10}\text{B} + {}^1n \rightarrow {}^7\text{Li} \,(1.015\ \text{MeV}) + {}^4\alpha \,(1.777\ \text{MeV}) \quad 6\% \tag{1a}$$

$$^{10}\text{B} + {}^1n \rightarrow {}^7\text{Li}^* (0.840\ \text{MeV}) + {}^4\alpha^* (1.470\ \text{MeV}) \quad 94\% \tag{1b}$$

The daughter particles (α particles and ^{7}Li ions) produced by the above nuclear reactions have large kinetic energies. The range is $\sim$5 µm for α particles and $\sim$2 µm for ^{7}Li ions in h-BN [11]. These particles deposit their kinetic energies in the h-BN semiconductor and subsequently generate many electron–hole pairs in h-BN, which serve as the detection signal for thermal neutrons. In comparison with commercial available neutron detectors based on ^{3}He gas, which has a thermal neutron cross-section $\sim$5330 barns [11,12], the atomic density of ^{3}He gas is significantly lower than that of ^{10}B in solids such as in h-BN thin films. Thus, the thermal neutron absorption length of ^{3}He is much larger than that of h-BN. On the other hand, the unique properties that set h-BN material apart from

* Corresponding author.
    E-mail address: hx.jiang@ttu.edu (H.X. Jiang).

direct conversion neutron detectors based on amorphous B_4C [23], gadolinium complexes [24], pyrolytic and polycrystalline BN, and alpha rhombahedral boron complexes [25,26] include: (1) h-BN has a simple crystal structure, which allows for the attainment of single crystalline thin films by epitaxial growth techniques such as metal organic chemical vapor deposition (MOCVD). Materials with single crystalline structure contain few charge traps and allow a rapid sweep-out of the electrons and holes generated by the nuclear reaction and high charge collection efficiency. To our knowledge, all prior reported direct conversion neutron detectors incorporate non-single crystalline compounds. Due to the material's porosity and disordered nature, the charge collection efficiency in prior direct conversion devices was limited. (2) ^{10}B-enriched h-BN layers have a low thermal neutron absorption length of 47 μm [10]. (3) Its unique layered structure provides very excellent lateral transport proper-ties and allows for the construction of lateral devices with very high charge collection efficiency. (4) It has very favorable basic parameters including extremely low dark current (as low as 10^{-11} A/cm^2 at a bias voltage of 10 V) due to its large energy bandgap of around 6.4 eV [1–5] and its high resistivity [4,10]. This capability allows for the construction of large area detectors with low dark counts and high sensitivity. (5) Large area wafers and large area detectors are possible. Since h-BN is a wide bandgap semiconductor and a member of the III–nitride family, the development of h-BN materials heavily leverages the scientific knowledge of III–nitride semiconductors. If we adopt the large-scale MOCVD growth systems available today for the production of III–nitride materials and light emitting diode wafers, large h-BN wafers can be produced, which would enable the fabrication of large area h-BN neutron detectors at a relatively low cost.

Based on our previous studies [9,10], the focus of this work is on improving the material quality, with particular emphasis on improving the basic material properties of h-BN epilayers that are important for the design of neutron detectors, including the crystalline quality and carrier mobility-lifetime (μτ) product and diffusion length (L_D). Metal-semiconductor-metal (MSM) thermal neutron detectors based on h-BN thin films have been fabricated. The reaction product pulse height spectra of h-BN MSM detectors were measured under thermal neutron irradiation produced by a ^{252}Cf source moderated by a high density polyethylene (HDPE) block. Very narrow individual peaks corresponding to the reaction product energies of α and Li particles as well as the sum peaks have been clearly resolved in the pulse height spectrum for the first time by a B-based direct-conversion semiconductor neutron detector.

2. Material growth and basic material properties

The h-BN thin film structure employed in this study, which was grown by MOCVD on a c-plane sapphire substrate using triethyboron (TEB) and ammonia (NH$_3$) as B and N sources, respectively [3–5], is shown in Fig. 1(a). The films were grown at 1350 °C using hydrogen as a carrier gas. For h-BN epilayer growth, the parasitic reaction between TEB and NH$_3$ in the gas phase may pose a problem [27]. This reaction resembles the reaction between NH$_3$ and TMAl during AlN epilayer growth [28]. The surface migration of boron atoms is poor because of the strong B–N bond and a severe parasitic reaction between TEB and NH$_3$. The by-products of the pre-reaction could cause a rough surface and introduce defects in the wafer. Therefore, we adopted from the growth of AlN a pulsed precursor flow epitaxy to control the growth kinetics [27,28]. In this case, NH$_3$ and TEB precursors were separately injected into the MOCVD reactor. This significantly suppressed the parasitic reactions in the gas phase. In comparison to our previous studies [9,10], we have further optimized the pulsed growth parameters such as "on" time for NH$_3$ flow and "on" time for TEB flow. However, there are several other growth
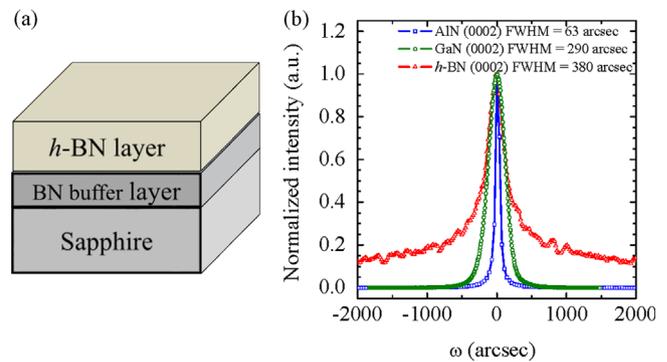
(a)

(b)

Fig. 1. (a) Schematic of layer structure of h-BN thin films used in this work and (b) comparison of XRD rocking curves (ω scans) of (0002 peak) among h-BN, AlN, and GaN.

parameters including the TEB and NH$_3$ flow rates, growth tempera-ture, and reactor pressure, V/III ratio and hence there continues to be a need to optimize epitaxial growth processes to produce materials with improved quality. The as-grown films are highly resistive with an estimated room temperature resistivity of $\rho \approx 5 \times 10^{10}$ Ω cm. X-ray diffraction (XRD) results showed that these h-BN films are single crystals of hexagonal phase [3]. The peak positions of θ–2θ scans revealed that h-BN epilayer has a c-lattice constant of about 6.67 Å, which is very close to the c-lattice constant of h-BN bulk (6.66 Å) [29,30]. Fig. 1(b) compares the XRD rocking curves (ω-scan) of the (0002) diffraction peaks between MOCVD grown h-BN, GaN, and AlN epilayers with a comparable thickness produced by our group, all deposited on sapphire substrates. The full width at half maximum (FWHM) of the h-BN (0002) rocking curve is ∼380 arcsec. In comparison with other III–nitride materials, the FWHM of XRD rocking curve of h-BN epilayers is 5–8 times broader than those of high quality AlN epilayers deposited on c-plane sapphire (around 60 arcsec) [31]. These results indicate that further improvements in growth processes are still required. In III–nitride materials, it is well known that the FWHM of XRD rocking curves is correlated with the density of dislocations. In the case of h-BN with layered structure, the FWHM could also reflect the presence of misalignment between layers, stacking faults and native defects. However, because the FWHM of XRD rocking curves of h-BN are comparable to those of typical GaN epilayers deposited on c-plane sapphire (around 300 arc-sec) [32], the crystalline quality of the present h-BN films is sufficient for device demonstration. For device demonstration, we selected a film thickness of 0.3 μm. Since the development of h-BN epilayers is still in its early stage, the surface morphology of h-BN epilayers becomes poorer with increasing the h-BN layer thickness. Therefore, in selecting the h-BN epilayer thickness for detector fabrication, we considered the trade-off between ensuring the highest material quality (fewer charge carrier traps) and a sufficient layer thickness for appreciable thermal neutron absorption.

Another very important parameter that characterizes the electro-nic quality of a semiconductor for detector fabrication is its charge carrier mobility-lifetime (μτ) product. The μτ product determines the average distance traveled by the free carriers per unit electric field before recombination or trapping occurs. Most of the free carriers can be collected by the electrodes if the recombination or trapping time (τ) is larger than the transit time (τ_t), $\tau > \tau_t (= L/\mu E)$, or equivalently, the minimum acceptable μτ product is $\mu\tau \geq (L/E)(\mathrm{cm}^2/V)$, where E is the applied electric field and L is the distance between two electrodes [33]. Increasing the μτ product ultimately will enhance the efficiency of charge collection and hence the performance of the fabricated detector. This parameter is significantly influenced by the density of impurities/defects intro-duced during the crystal growth which act as charge carrier traps.
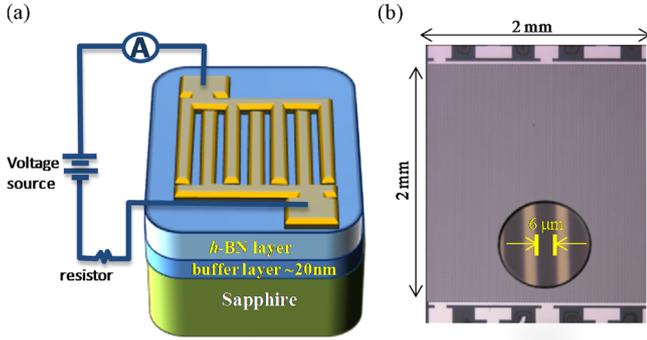
Fig. 2. (a) Schematic illustration of h-BN MSM detector and the setup for the I–V characteristics measurements. (b) Optical microscopy image of a fabricated MSM detector with a device size of 2 mm × 2 mm and 6 μm/6 μm finger width/spacing and h-BN film thickness of 0.3 μm.

To characterize the μτ products, metal-semiconductor-metal (MSM) detectors with micro-strip inter-digital fingers were fabricated from h-BN epilayers for I–V characterization, as shown in Fig. 2. Micro-strips patterns were defined by photolithography and pattern transfer was accomplished by inductively coupled plasma (ICP) dry etching using SF_6 based chemistry [34]. The MSM detectors have dimensions of 2 mm × 2 mm. The width of the metal finger is about 6 μm while the spacing between the fingers is about $L=6$ μm. A Ti/Al bilayer (20 nm/30 nm) was deposited by e-beam evaporation as the metal contacts. The etched strip geometry allows the device to effectively utilize the excellent lateral transport properties within the basal planes in h-BN.

To obtain the μτ products, a broad spectrum light source (LDLS, EQ-99 by Energetiq) was used to illuminate the whole area of the h-BN MSM device. Under photo-excitation, photo-generated electrons and holes are drifted to the electrodes under the applied electric field. The I–V characteristics are described by the modified Many's equation [35,36]

$$I(V) = I_o \left[\frac{\mu_e \tau_e V}{L^2} - \left(\frac{\mu_e \tau_e V}{L^2} \right)^2 \left(1 - e^{-\frac{L^2}{\mu_e \tau_e V}} \right) \right.$$
$$\left. + \frac{\mu_h \tau_h V}{L^2} - \left(\frac{\mu_h \tau_h V}{L^2} \right)^2 \left(1 - e^{-\frac{L^2}{\mu_h \tau_h V}} \right) \right] \quad (2)$$

where V is applied bias voltage and L is the distance between two electrodes, $\mu_e \tau_e$ and $\mu_h \tau_h$ are the mobility-lifetime product of electrons and holes, respectively. I_o is the saturation current. The first (last) two terms are the contributions of the photo-generated electrons (holes) and μτ products for electrons and holes can thus be obtained by fitting the measured I–V curve with Eq. (2). In Fig. 3, we plot the I–V characteristics for a representative h-BN MSM device under light illumination, which shows that the photocurrent increases with an increase of the applied electric field $E\ (=V/L)$ and it approaches to a saturation value at E $\sim 2.5 \times 10^4$ V/cm.

In applying Eq. (2), we assumed that $\mu_e \tau_e = \mu_h \tau_h$ for h-BN. This assumption is based on the fact the dispersions for the electrons and holes are identical and holes are truly anti-particles of electrons in single sheet h-BN [37–39]. This means that electrons and holes have an identical effective mass in single sheet h-BN [38]. Although the h-BN epilayers are three-dimensional systems, the charge carriers can be treated approximately as if they are transporting through a stack of independent layers of a 2D structure [40–42]. Therefore, we believe that to the first order the assumption of $\mu_e \tau_e = \mu_h \tau_h$ for h-BN epilayers is valid. In Fig. 3, the solid curve is the least squares fit of experimental data (open squares) with Eq. (2). The fitted μτ products of electrons and holes are $\mu_e \tau_e = \mu_h \tau_h = 2.83 \times 10^{-7}$ cm²/V. The diffusion length L_D can also be obtained from the measured μτ
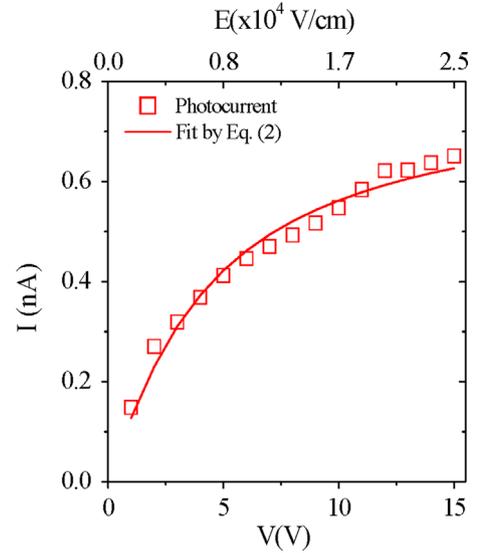
Fig. 3. I–V characteristics of an h-BN MSM detector under light illumination or photo-current (I) versus bias voltage (V). Squares are the measured data and the solid curve is the least squares fitting of data with Eq. (2). The size of the squares indicates the error bar size of the data points.
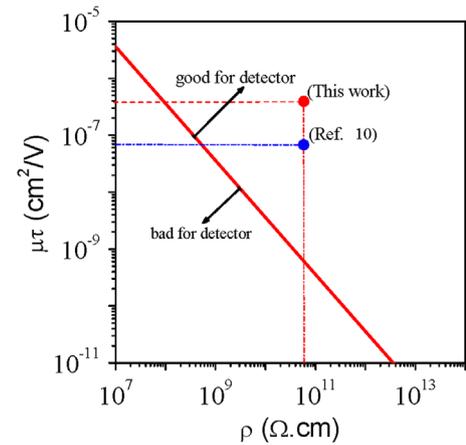

Fig. 4. Plot of the minimum acceptable mobility-lifetime product versus resistivity for h-BN epilayers. The measured electron μτ products are also included in the plot for the present work and a previous work [Ref. 10].

products using Einstein's equation

$$L_D = \sqrt{\frac{k_B T}{q} \mu \tau} \quad (3)$$

where $k_B = 1.38 \times 10^{-23}$ (m² kg s⁻² · K⁻¹) is the Boltzmann constant, T is temperature, and $q = 1.6 \times 10^{-19}$ (C) is the electron charge. $L_D = 0.86$ μm (for both electrons and holes) are obtained from Eq. (3). Fig. 4 is a plot of the minimum acceptable μτ product as a function of the sample resistivity for h-BN [10]. The $\mu_e \tau_e$ product values of electrons are indicated as dots in Fig. 4 for the h-BN epilayers used in the present work and also for those reported in our previous work [10]. Although both data points fall into the area above the straight line (or above the minimum acceptable values), the results indicate that we have achieved an enhancement in μτ product by a factor of more than 6 for films with a comparable electrical resistivity ($\rho \approx 5 \times 10^{10}$ Ω cm). The improvements are primarily attributable to the optimization of MOCVD growth processes. In comparison, the $\mu_e \tau_e$ product reported for GaN thin films with a resistivity of about 5×10^7 Ω cm is around 10^{-7} cm²/V [43]
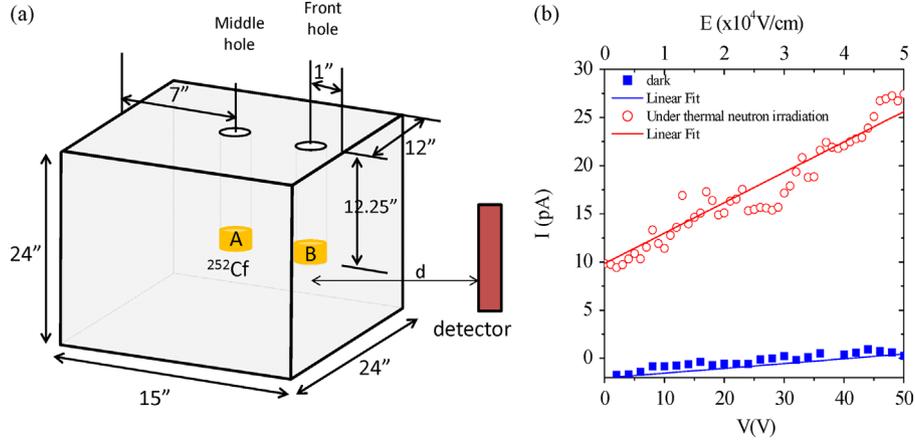
Fig. 5. (a) Schematic diagram of the thermal neutron source [produced by ^{252}Cf in conjunction with a high-density-polyethylene (HDPE) moderator] utilized in this study, where *d* is the distance between the detector and the moderator surface. (b) *I–V* characteristics of an *h*-BN MSM detector in the "dark" (in the absence of thermal neutron source) and under thermal neutron irradiation. The MSM detector used has a dimension of 2 mm × 2 mm and was placed 3 cm array from the ^{252}Cf source (or *d*=0 cm from the front surface of the HDPE moderator).
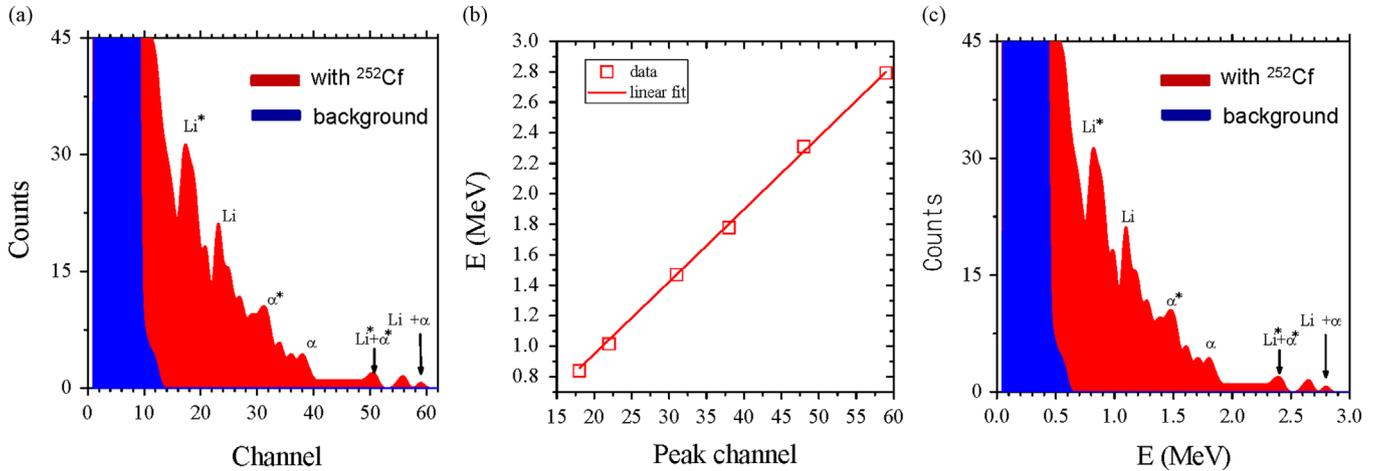
Fig. 6. Nuclear reaction pulse height spectrum measured with an *h*-BN MSM neutron detector biased at 20 V for 7 h. Blue—background counts; Red—under neutron irradiation produced by a ^{252}Cf source in conjunction with a HPDE moderator. (a) Counts versus channel number, (b) energy peak calibration among all expected nuclear reaction products, and (c) counts versus energy (MeV). The MSM detector used for pulse height spectrum measurement has a device size of 3 mm × 4 mm and 6 μm/6 μm finger width/spacing and *h*-BN film thickness of 0.3 μm. The detector was placed 12 cm array from the ^{252}Cf source (or *d*=9 cm from the front surface of the HDPE moderator) as schematically indicated in Fig. 5(a). (For interpretation of the references to color in this figure legend, the reader is referred to the web version of this article.)

and for GaN nanowires with low defects is about 1.6×10^{-6} cm^2/V [44]. A comparison of the results implies that μτ values of *h*-BN are comparable or getting very close to those of GaN. Since the development of *h*-BN epilayers is still in an early stage, we anticipate that μτ products will continue to increase with further development in the growth processes.

3. Thermal neutron detection

As schematically illustrated in Fig. 5(a), a Californium-252 source (^{252}Cf) of 2.94 μg corresponding to 1.6 mCi of radiation activity was used as a neutron source. The source emits $\sim 7.0 \times 10^6$ neutrons/second with an average energy at about 2 MeV and a half-life of 2.65 years. A high-density-polyethylene (HDPE) moderator was constructed and used for converting fast neutrons emitted from ^{252}Cf to thermal neutrons [10,20,21]. The flux of thermal neutron is about 3.2×10^4 thermal neutrons/cm^2 s at the front surface of the HDPE moderator (or *d*=0 cm), which is 3 cm from the ^{252}Cf source. The *I–V* characteristics of the *h*-BN MSM neutron detector were measured in two different configurations: the detector was placed (a) very far away from and (b) in front of the HPDE moderator at *d*=0 cm (3 cm away from the ^{252}Cf source), which effectively corresponds to the

cases of (a) "dark" *I–V* characteristic (or in the absence of the neutron source) and (b) *I–V* characteristic in response to thermal neutron irradiation. Fig. 5(b) compares the *I–V* characteristics of the *h*-BN detector measured under the conditions of (a) under dark (blue squares) and (b) under thermal neutron irradiation (red open circles). The neutron generated current (ΔI) or the detector sensitivity increases linearly with the applied voltage (*V*). This can be understood if we express ΔI as follows:

$$\Delta I = A \times \Delta J = A(\sigma_e E + \sigma_h E) = AE(e \Delta n_e \mu_e + e \Delta p_h \mu_h) = AeE \Delta n_e (\mu_e + \mu_h)$$
(4)

where *A* is the cross-section area of current flow, E ($= V/L$) the applied electric filed, Δn_e and Δp_h ($\Delta n_e = \Delta p_h$) are the numbers of the neutron generated free electrons and free holes, and μ_e (μ_h) is electron (hole) mobility. A linear relationship between ΔI and *V* or E ($= V/L$) is thus expected before saturation. The slope of the plot depends on the number of charge carriers ($\Delta n_e = \Delta p_h$) generated under thermal neutron irradiation as well as the carrier mobility, which depend strongly on the materials quality.

To examine the impact of improved μτ products on the neutron detector performance, the pulse-height spectra were measured under thermal neutron irradiation produced by the ^{252}Cf source
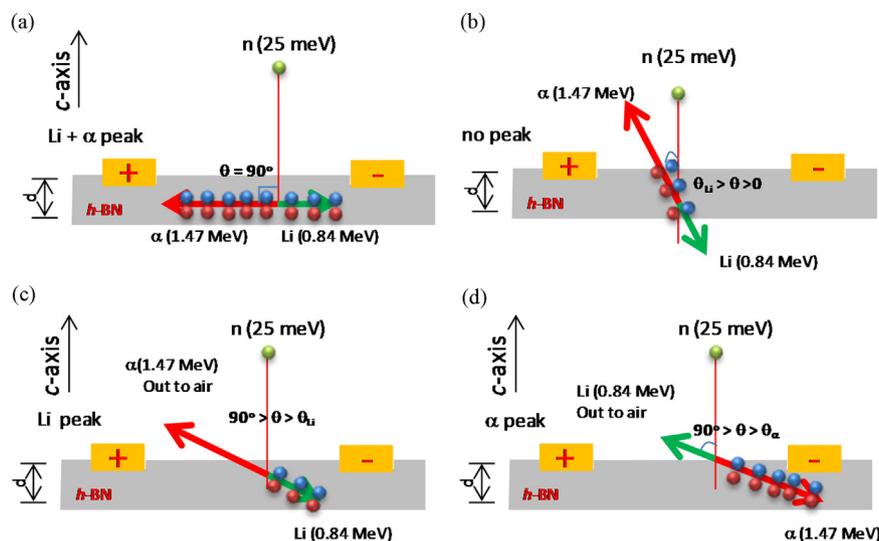
Fig. 7. Schematic illustration describing the mechanisms for observing (a) the Li+α peak; (b) no peak; (c) the Li peak; and (d) the α peak in the pulse height spectra obtained by *h*-BN thin film neutron detectors.

moderated by the HDPE block. The MSM detector used for pulse height spectrum measurement has a device size of 3 mm × 4 mm and *h*-BN film thickness of 0.3 μm. The width/spacing of the metal finger is 6 μm. The detector was enclosed by a shielding box to reduce the electronic noise and placed 12 cm array from the ^{252}Cf source (or *d* = 9 cm from the front surface of the HDPE moderator). The pulse-height spectra were obtained using a multi-channel analyzer (MCA) (model 8000D by Amptek) in conjunction with a charge sensitive modified preamplifier (model CR-110, Cremat, Inc.) having a rise time of 7 ns and decay time constant of 140 μs and a pulse shaping amplifier (model CR-200, Cremat, Inc.) having a shaping time 2 μs. The blue and red column bars in Fig. 6(a) are the total counts measured in the absence and presence of the ^{252}Cf source, respectively. In the absence of the ^{252}Cf source, the counts are just background noise. The measured pulse-height spectra under thermal neutron irradiation show very well resolved peaks corresponding to all the product energies of ^{10}B and thermal neutron reaction described in Eq. (1), including Li, Li*, α, and α* peaks as well as the sum peaks Li+α and Li*+α*. This series of nuclear reaction product energy peaks are resolved much more prominently than our previous reported results [10], attributing to the reduced charge carrier traps and hence the charge collection efficiency in the *h*-BN materials, which is reflected in the enhanced μτ product. The calibration between energy and channel number for the whole spectrum is plotted in Fig. 6(b), which shows a linear relationship between the reaction product energies of Li*, Li, α*, α, Li*+α*, and Li+α peaks and the channel numbers, exactly according to the values expected from Eq. (1). The open squares in Fig. 6(b) are the data points and the solid straight line is the linear fit. In Fig. 6(c), we re-plot the pulse height spectrum in the energy scale. This perfect agreement between the experimental data and expected energy peaks of nuclear reaction products of Eq. (1) shown in Fig. 6(b) in turn provides a great confidence in our assignment of the observed peaks in the pulse-height spectrum. It is remarkable that *h*-BN thin film detectors are capable to resolve specific nuclear reaction products with such a high energy resolution. For instance, the energy resolution at 1.015 MeV (^{7}Li peak) is around 100 keV. This unique aspect can be understood by considering the fact that the nuclear reaction and free charge carrier generation and collection occur in the same *h*-BN layer that is a single crystal material.

The schematic diagrams in Fig. 7 illustrate how all the individual reaction product peaks (α, α*, Li, Li*, Li+α and Li*+α*) are being resolved. One of the primary reasons for the *h*-BN detector to resolve

all the reaction product peaks is that the layer thickness of *h*-BN used in the detector is much less than the α and Li particle ranges in *h*-BN. As schematically shown in Fig. 7(a), the sum peak corresponds to the case in which both α and Li (α* and Li*) particles are moving almost in the plane or *θ* = 90°, which is a very low-probability event in an *h*-BN layer with a thickness much smaller than the ranges of α and Li particles. Fig. 7(b) illustrates the most probable situation or highest probability event in which both α and Li particles only deposit part of their energies in the detector and thus do not register any counts at their respective energy positions in the pulse height spectrum. Fig. 7(c) represents the case that a Li particle deposits all its energy in the detector and hence registers the Li peak on the spectrum. In the reverse situation as shown in Fig. 7(d), an α particle depositing its whole energy in the detector and hence registering the α peak on the spectrum. It is expected that the scenario shown in Fig. 7(a) will be the most probable event and the pulse-height spectrum will consist of predominantly the sum peaks once we incorporate *h*-BN layer with a thickness which is larger than the ranges of α and Li particles in *h*-BN (~5 μm). However, the high energy resolution feature will be retained because the nuclear reaction and free charge carrier generation and collection occur in the same crystalline *h*-BN epilayer.

It is apparent that the energy resolution of the reaction products is directly correlated with the crystalline quality and is expected to continue to improve with further improvement in the material quality (reduction in the density of charge carrier traps) of the *h*-BN films. It should be noted that our *h*-BN films are grown on foreign substrate (sapphire). As such, the complete elimination of charge carrier traps (dislocations, stacking faults and native defects) is very difficult. Therefore, the energy resolution of thermal neutron and ^{10}B reaction products resolved by *h*-BN thin film detectors is expected to be less sharp than those of standard α particle detectors based on bulk Si which is the most developed among all semiconductors. Although pure α particle detectors based on Si are not useful as thermal neutron detectors, for benchmarking purpose, the energy resolution of ORTEC's Si based α particle detectors can be as low as several to tens of keV at 5.486 MeV (^{241}Am).

We note that boron thin film coated GaAs indirect-conversion detectors were able to resolve spectral features of the 1.47 MeV (α) and 0.84 MeV (Li) peaks with an energy resolution of about 300 keV at 0.84 MeV [15,16]. On other hand, the signals of the sum peaks have been detected by various types of solid-state detectors [17–24]. However, the spectral feature was greatly distorted with no energy resolution either due to charge carrier trapping in direct-conversion

devices based on amorphous or polycrystalline materials or due to the random path lengths of ^{7}Li and α particles involved in ^{10}B-perforated Si pillar based indirect-conversion detectors. In boron perforated indirect-conversion devices [17–22], the ^{7}Li and α particles created in the conversion layer must travel a certain distance before reach to the semiconductor layer to generate electrons and holes. During this process, ^{7}Li and α particles loss a certain fraction of their energies depending on the path lengths which are random. Therefore, the spectral features of reaction products in the pulse-height spectra of boron perforated indirect-conversion devices generally are broadened due to this energy dispersion process. On the other hand, due to the material's porosity and disordered polycrystalline nature [23,24], the charge carrier trapping is severe in direct conversion detectors based on amorphous or polycrystalline thin films, which also renders the pulse-height spectra with no energy resolution. In this sense, semiconductor detectors based on single crystal h-BN are much more sensitive to resolve energies of specific reaction products than indirect-conversion devices or direct conversion detectors based on non-single crystalline materials.

We believe that the distinct feature of high energy resolution of the reaction products potentially provides the following unique advantages: (a) *High sensitivity and low noise*—The high energy resolution feature of specific products of the thermal neutron and ^{10}B nuclear reaction (e.g., the sum peaks at 2.31 MeV and 2.79 MeV) can be used to effectively discriminate detector's responses to all other types of radiation. (b) *Simple read out electronics*—Since we only need to record counts around the energies of specific reaction products (e.g., around the sum peaks at 2.31 MeV and 2.79 MeV), we do not need to use MCA to add up all counts at different energies above a certain threshold. A simple circuit consisting of a discriminator with lower and upper thresholds covering these energy regions will be sufficient. By setting lower and upper level discriminators that bound those sum peaks, the overall efficiency may be slightly reduced. However, the high energy resolution of the reaction products provides an opportunity to design thermal neutron detectors with extremely low background counts and correspondingly low false alarm rate at the cost of slightly reduced overall detection efficiency. There are many application areas where detectors with low false alarm rates are preferred. Another obvious advantage of h-BN neutron detectors is the low bias operating voltage (e.g., $V=20$ V in Fig. 6), which makes the design and operation of h-BN detectors much more convenient and versatile than other types of neutron detectors.

4. Summary

In summary, solid-state thermal neutron detectors have been fabricated from h-BN thin films. In comparison to our previously reported results [10], the mobility-lifetime ($\mu\tau$) products were significantly improved. The measured $\mu\tau$ product of electrons and holes is about 2.83×10^{-7} cm^2/V. The reaction product pulse-height spectra were measured under thermal neutron irradiation produced by a ^{252}Cf source moderated by a high density polyethylene block. The measured pulse-height spectra revealed very narrow peaks corresponding to the product energies of ^{10}B and neutron reaction, including indiviual α and Li peaks as well as the α+Li sum peak. We believe that these unique features together with thin film nature of h-BN can be used to construct highly compact neutron detectors with very high specificity and sensitivity. Further improvements in material quality are still needed. In particular, there is a need to further develop thin film growth processes to produce high quality h-BN films with a large layer thickness. The calculated thermal neutron absorption length of h-^{10}BN is 47 μm [10]. For an h-^{10}BN layer with thickness of $t=35$ μm, the fraction of the absorbed thermal neutrons is 50%. Based on the sharp spectral feature of the reaction products, the charge collection efficiency in h-BN

detectors is very high. Therefore, thermal neutron detectors with high efficiencies can be realized from h-^{10}BN semiconductor epitaxial layers with large thicknesses. Together with the ability of producing wafer scale h-BN semiconductor materials by techniques such as MOCVD and the applicability of semiconductor processing technologies, the features of high charge collection efficiency and high energy resolution of the reaction products of h-BN detectors open up the possibility to construct sophisticated neutron detectors with high sensitivity at relatively low costs.

References

[1] K. Watanabe, T. Taniguchi, H. Kanda, Nature Materials 3 (2004) 404.
[2] K. Watanabe, Takashi Taniguchi, T. Niiyama, K. Miya, M. Taniguchi, Nature Photonics 3 (2009) 591.
[3] R. Dahal, J. Li, S. Majety, B.N. Pantha, X.K. Cao, J.Y. Lin, H.X. Jiang, Applied Physics Letters 98 (2011) 211110.
[4] J. Li, S. Majety, R. Dahal, W.P. Zhao, J.Y. Lin, H.X. Jiang, Applied Physics Letters 101 (2012) 171112.
[5] S. Majety, X.K. Cao, J. Li, R. Dahal, J.Y. Lin, H.X. Jiang, Applied Physics Letters 101 (2012) 051110.
[6] N. Alem, R. Erni, C. Kisielowski, M.D. Rossell, W. Gannett, A. Zettl, Physical Review B 80 (2009) 155425.
[7] C.R. Dean, A.F. Young, I. Meric, C. Lee, L. Wang, S. Sorgenfrei, K. Watanabe, T. Taniguchi, P. Kim, K.L. Shepard, J. Hone, Nature Nanotechnology 5 (2010) 722.
[8] A.K. Geim, I.V. Grigorieva, Nature 499 (2013) 419.
[9] J. Li, R. Dahal, S. Majety, J.Y. Lin, H.X. Jiang, Nuclear Instruments and Methods in Physics Research A 654 (2011) 417.
[10] T.C. Doan, S. Majety, S. Grendadier, J. Li, J.Y. Lin, H.X. Jiang, Nuclear Instruments and Methods in Physics Research A 748 (2014) 84.
[11] G.F. Knoll, Radiation Detection and Measurement, 4th edition, John Wiley & Sons, Hoboken, New Jersey, USA, 2010.
[12] O. Osberghaus, Zeitschrift fuer Physik 128 (1950) 366.
[13] Physics Today 64, 20, 2011.
[14] http://www.dhs.gov/news/2014/07/29/written-testimony-dndo-house-homeland-security-subcommittee-cybersecurity.
[15] D.S. McGregora, R.T. Klann, H.K. Gersch, Y.H. Yang, Nuclear Instruments and Methods in Physics Research A 466 (2001) 126.
[16] D.S. McGregor, J.K. Shultis, Nuclear Instruments and Methods in Physics Research A 517 (2004) 180.
[17] R.J. Nikolic, C.L. Cheung, C.E. Reinhardt, T.F. Wang, Proceeding SPIE 6013 (2005) 601305.
[18] R.J. Nikolic, A.M. Conway, C.E. Reinhardt, R.T. Graff, T.F. Wang, N. Deo, C.L. Cheung, Applied Physics Letters 93 (2008) 133502.
[19] S.L. Bellinger, W.J. McNeil, T.C. Unruh, D.S. McGregor, IEEE Transaction Nuclear Science NS-56 (2009) 742.
[20] J. Clinton, Optimization and Characterization of a Novel Self Powered Solid State Neutron Detector Doctoral Thesis, Rensselaer Polytechnic Institute, New York, USA (2011) 73–78, Chap. 3.
[21] R. Dahal, K.C Huang, J. Cliton, N. LiCausi, J.-Q. Lu, Y. Danon, I. Bhat, Applied Physics Letters 100 (2012) 243507.
[22] Q. Shao, L.F. Voss, A.M. Conway, R.J. Nikolic, M.A. Dar, C.L. Cheung, Applied Physics Letters 102 (2013) 063505.
[23] K. Osberg, N. Schemm, S. Balkir, J.O. Brand, M.S. Hallbeck, P.A. Dowben M.W. Hoffman, IEEE Sensors Journal 6 (2006) 1531.
[24] Y.B. Losovyj, I. Ketsman, A. Sokolov, K.D. Belashchenko, P. Dowben, J. Tang, Z. Wang, Applied Physics Letters 9 (2007) 1132908.
[25] D.S. McGregor, T.C. Unruh, W.J. McNeil, Nuclear Instruments and Methods in Physics Research A 591 (2008) 530.
[26] A.N. Caruso, J. Physics: Condensed Matter 22 (2010) 443201.
[27] H.X. Jiang, J.Y. Lin, Semiconductor Science Technology 29 (2014) 084003.
[28] M.A. Khan, J.N. Kuznia, R.A. Skogman, D.T. Olson, M.M. Millan, W.J. Choyke, Applied Physics Letters 61 (1992) 2539.
[29] R.W. Lynch, H.G. Drickamer, Journal of Chemical Physics 44 (1966) 181.
[30] R.S. Pease, Acta Crystallographica 5 (1952) 356.
[31] B.N. Pantha, R. Dahal, M.L. Nakarmi, N. Nepal, J. Li, J.Y. Lin, H.X. Jiang Q.S. Paduano, D. Weyburne, Applied Physics Letters 90 (2007) 241101.
[32] S. Nakamura, G. Fasol, S.J. Pearton, The Blue Laser Diode: The Complete Story, Springer, New York, 2000.
[33] W.C. Mcginnis, R. Clarke, C. Cionca, and R. Brockus, Film Implementation of a neutron detector (FIND): Critical Materials properties Technical Report, 2007.
[34] S. Grenadier, J. Li, J.Y. Lin, H.X. Jiang, Journal of Vaccume Science and Technology A 31 (2013) 061517.

[35] A. Many, Journal of Physics and Chemistry of Solids 26 (1965) 575.

[36] Y. Nemirovsky, A. Ruzin, G. Asa, J. Gorelik, Journal of Electronic Materials 25 (1996) 8.

[37] P.R. Wallace, Physical Review 71 (1947) 622.

[38] G.W. Semenoff, Physics Review Letters 53 (1984) 2449.

[39] X.K. Cao, B. Clubine, J.H. Edgar, J.Y. Lin, H.X. Jiang, Applied Physics Letters 103 (2013) 191106.

[40] L.K. Gallos, A.N. Anagnostopoulos, P. Argyrakis, Physical Review B50 (1994) 14643.

[41] R. Fivaz, E. Mooser, Physical Review 136 (1964) A833.

[42] Optical and Electrical Properties," edited by P. L. Lee, (D. Reidel, Boston, 1976.

[43] M. Misra, D. Korakakis, H.M. Ng, T.D. Moustakas, Applied Physics Letters 74 (1999) 2203.

[44] P. Parkinson, C. Dodson, H.J. Joyce, K.A. Bertness, N.A. Sanford, L.M. Herz M.B. Johnston, Nano Letters 12 (2012) 4600.